Editors' Suggestion

Effect of capillary number and viscosity ratio on multiphase displacement in microscale pores

Samantha A. McBride,[1,*] Fernando Temprano-Coleto,[1,2,*] Paul R. Kaneelil,[1,3] Reese Knopp,[1] Aubrey J. Taylor,[1] Mariko A. Storey-Matsutani,[1] Jessica L. Wilson,[1] Mohammad Sadeq Saleh,[1] Andrew R. Konicek,[4] Arben Jusufi,[4] Mohsen S. Yeganeh,[4] and Howard A. Stone[1,†]

[1]*Department of Mechanical and Aerospace Engineering, Princeton University, Princeton, New Jersey 08544, USA*

[2]*Andlinger Center for Energy and the Environment, Princeton University, Princeton, New Jersey 08544, USA*

[3]*John A. Paulson School of Engineering and Applied Sciences, Harvard University, Cambridge, Massachusetts 02138, USA*

[4]*ExxonMobil Technology and Engineering Company, Annandale, New Jersey 08801, USA*

(Received 27 July 2023; accepted 4 March 2025; published 5 May 2025)

Understanding the dynamics of fluid transport and trapping within microscale cavities is important for a range of environmental, industrial, and research applications. Using PDMS microfluidic channels, we explore the displacement and retention of (wetting) oil by an invading flow of (nonwetting) water at low Reynolds number ($\mathrm{Re} \ll 1$) in noncontiguous pores, and examine the influence of trapping velocity, viscosity ratio, and pore aspect ratio. We find that increasing capillary numbers lead to a greater amount of oil trapped per cavity. This is contrary to findings for interconnected porous media in which the availability of multiple pathways for fluid flow leads to more displacement with increased flow rates. This result can be attributed to a dynamic transition from a meniscus displacement to a viscous fingering displacement, by which the advancing water front shifts from a discrete triple contact line at channel walls to a continuous layer of oil enveloping the water. Data from all pore geometries can be collapsed onto a single trend by subtracting the amount of oil captured in the zero capillary number limit, indicating that increased oil retention at higher values of capillary number is not dependent on pore geometry. A model for steady-state, three-dimensional flow based on the long-wave approximation was developed to analyze the amount of fluid retained as a function of capillary number and viscosity ratio. Model predictions are qualitatively consistent with several experimental observations, including the shape of the interface of the trapped oil and the trend that increasing capillary number leads to greater oil trapping per pore. Our results highlight the need to quantitatively investigate the transient dynamics of fluid invasion in multiphase systems that exhibit localized entrapment.

DOI: 10.1103/PhysRevFluids.10.054201

I. INTRODUCTION

Fluid transport and entrapment within cavities is significant for a range of environmental, industrial, and research applications [1,2]. In some applications such as lubricant impregnated surfaces, the aim is to maintain stable lubricant layers within a textured solid surface [3–5]. These

*These authors contributed equally to this work.
†Contact author: hastone@princeton.edu

materials can be used to reduce drag [6], prevent fouling [7,8], capture CO_2 [5], and enhance liquid mobility on surfaces [3]. Preening oil within bird feathers is one example of liquid infusion in nature. The stable oil barrier keeps water out of feathers and enables birds to more easily stay afloat [9]. In other applications, it is desirable to reduce or eliminate trapping of one liquid phase by another. For example, water can be used to dislodge oil trapped within porous shale rock for oil recovery [10].

Microfluidic devices enable control over multiphase phenomena including mixing of emulsions, controlling drop motion, and manipulating coalesence and mixing [2]. Some applications for microfluidic devices with trapped liquid cavities include diagnostics [11,12], microreactors for study of chemical kinetics [13,14], and understanding wettability dynamics of environmental processes such as CO_2 sequestration [15] and groundwater remediation [16]. Multiphase displacement flows in the presence of pores and obstacles in micromodels have been investigated previously [17–21], with the finding that displacement behavior is a function of the relative ratios of capillary, buoyant, and viscous forces [22]. When buoyancy is negligible (i.e., at low Bond numbers [23]) fluid entrapment and displacement within microscale pores are primarily dependent on the viscosity ratio between the two fluids, the pore geometry, and the wetting properties of the three phases (the trapped fluid, displacing fluid, and solid substrate) [18,19,24,25]. The wettability dynamics, viscosity ratio [26], and aspect ratio of the features [27] also determine the ability of a shear flow to displace a trapped phase, as well as flow dynamics within the pockets [28,29]. The capillary number is an especially important parameter in microporous multiphase displacement and describes the ratio between viscous and capillary forces: $\mathrm{Ca} = \mu V/\gamma$, where μ and V are the viscosity and velocity scale of one of the fluids, respectively, and γ is the interfacial tension between the fluid phases.

Multiphase displacement of water by an air bubble in a narrow capillary was previously described by Bretherton [30]. The Bretherton model describes how the thin film thickness of the displaced fluid varies as a function of capillary number (based on the displaced phase). At low Ca, the leading meniscus dominates such that the entirety of the displaced fluid is pushed out of the capillary. As Ca increases, a transition occurs in which viscous forces become more significant and a thin film of displaced fluid is left during bubble motion, with the thickness of this film scaling with $\mathrm{Ca}^{2/3}$. The decrease in the triple-phase contact angle and eventual transition to entrainment of a film of the displaced fluid is termed dynamic wetting [31,32]. The transition point where the film becomes entrained is a function of both Ca and the viscosity ratio between the displaced and displacing fluids λ. When the displacing liquid is more viscous, the thickness of the displaced liquid increases [33].

Oil recovery from porous matrices is one important application for understanding multiphase displacement dynamics in microscale capillaries. Micromodels simulating porous media flows have found that once a trapped fluid loses connectivity between adjacent pores, recovery of the fluid becomes challenging without altering the properties of the displacing fluid, such as via addition of surfactant [34,35]. In contrast, oil removal and trapping for disconnected cavities in capillaries is a strong function of three-phase wettability and pore geometry. In particular, the pore aspect ratio and the ratio between the pore opening length and the channel width dominate trapping [25,28] [Fig. 1(a) and Fig. 1(b)]. Pore geometry and roughness lead to altered displacement dynamics compared to smooth channels without texture [36].

In the present study, we investigate the entrapment of oil in disconnected sinusoidal pores across a wide range of capillary numbers defined using the viscosity of the oil phase ($10^{-5} \leqslant \mathrm{Ca_o} \leqslant 2 \times 10^{-2}$). Here the oil capillary number $\mathrm{Ca_o} = \mu_o V_f/\gamma$ was varied altering the flow rate of the displacing fluid (and therefore its front velocity V_f) and changing the viscosity μ_o of the displaced fluid. For all flow rates, the Reynolds number remained in the viscous regime ($\mathrm{Re} \ll 1$), and the fluid-fluid interfacial tension was kept constant. We use water as the displacing phase, which is nonwetting to the PDMS channels, and oil, which is wetting, as the trapped or displaced phase. These experiments examine the influence of capillary number, viscosity ratio, and pore geometry on retention of oil within the sinusoidal pores. In our disconnected porous microfluidic system, higher water intrusion velocities lead to more trapping of the wetting-phase oil. This is in contrast to interconnected porous micromodels, where multiple pathways for fluid flow lead to increased displacement of oil at higher flow rates [37–41]. We also find that increasing the ratio between the

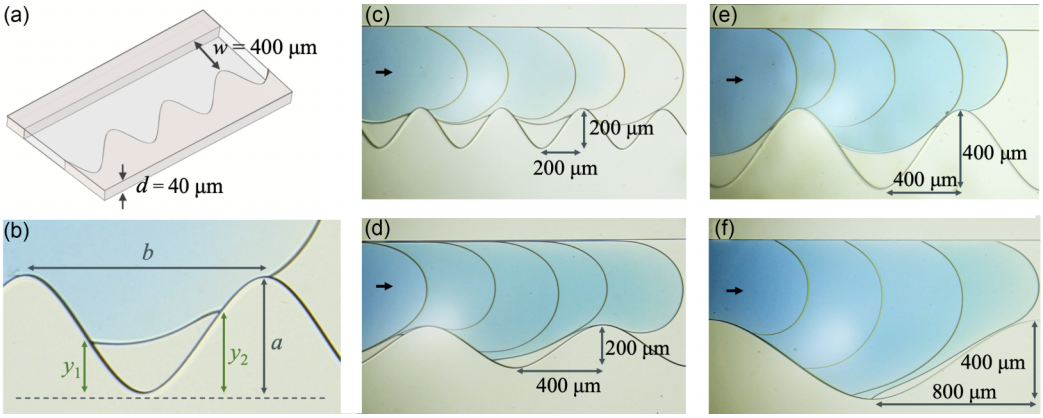

FIG. 1. Experimental geometry. (a) Schematic of microfluidic chips with one flat wall and one wall patterned with sinusoidal cavities. All devices have a channel width of 400 μm and a depth of 40 μm. (b) Definition of the wavelength, b, and height, a, of the sine geometry. (c)–(f) Overlay of images showing typical progression of the invading blue-dyed water for different geometries. Oil viscosity $\mu_o = 7.3 \times 10^{-2}$ Pa s ($\lambda = 73$). Arrows indicate flow direction. (c) $a = 200$ μm, $b/a = 2$, $V_f = 0.1$ mm/s. Time points from left to right are $t = 0$, 2, 6, 9, and 13 s. (d) $a = 200$ μm, $b/a = 4$, $V_f = 0.5$ mm/s. Time points from left to right are $t = 0$, 0.6, 1.2, 1.6, and 2.2 s. (e) $a = 400$ μm, $b/a = 2$, $V_f = 0.05$ mm/s. Time points from left to right are $t = 0$, 5, 12, 24, and 28 s. (f) $a = 400$ μm, $b/a = 4$, $V_f = 0.65$ mm/s. Time points from left to right are $t = 0$, 0.9, 1.9, and 2.7 s.

viscosities of displaced oil and intruding water ($\lambda = \mu_o/\mu_w$) increases oil trapping in pores. These results can be attributed to a transition from a meniscus regime with a three-phase contact line to a viscous thin film regime at higher intrusion velocities and at larger oil viscosities [42].

We also explore the role of the sinusoidal pore geometry, namely, the ratio of pore wavelength to pore depth, on oil displacement. Previous work demonstrated that this ratio predicts oil residual volumes at lower intrusion velocities [25]. At low capillary numbers and a moderate viscosity ratio ($Ca_o < 10^{-5}$, $\lambda = 1$), the amount of oil retained depends primarily on the equilibrium contact angles between the three phases and on the geometry of the pores [25]. This baseline amount of trapped oil can be regarded as a "zero capillary number" limit. We find that, as the capillary number increases from this limit, the pore aspect ratio has a negligible effect on the amount of oil trapped beyond this baseline amount. Thus, while pore geometry determines the baseline oil captured in the zero capillary number limit [25], it has limited influence on the extra amount captured at higher values of Ca_o and λ.

II. METHODS

Microfluidic devices were fabricated from PDMS (polydimethylsiloxane) cured on silicon master templates coated with 1H,1H,2H,2H-trichlorooctylflourosilane (Sigma) to facilitate PDMS removal. All channels were 40 μm deep (d) with a channel width (w, defined as the distance between the flat wall and the peak of the sine geometries, i.e. the smallest width) of 400 μm, as shown in Fig. 1(a). The wavelength between sine peaks is denoted b while the amplitude is denoted a, as shown in Fig. 1(b). We elected to keep the width and depth of the channel constant, as the critical dynamics in these experiments will depend on the ratio between viscous forces and surface forces, which are captured by the capillary number. Changing the width of the channel without altering the flow velocity (i.e., by increasing flow rate) should therefore still lead to the same wetting dynamics.

Four different sine geometries were used: $a = 200$ μm, $b/a = 2$ [Fig. 1(c)], $a = 200$ μm, $b/a = 4$ [Fig. 1(d)], $a = 400$ μm, $b/a = 2$ [Fig. 1(e)], and $a = 400$ μm, $b/a = 4$ [Fig. 1(f)]. Microfluidic devices were first filled with a wetting oil (Krytox GPL). An aqueous solution of 0.1% wt methylene blue was prepared using DI water purified with a Milli-Q Direct Water Purification System

TABLE I. Minimum amount of oil trapped in the low Ca_o limit (A_o) compared to maximum pore size A_{max} and the ratio of these ($\tilde{A}_o$) for each of the four geometries.

a	b/a	$A_o(mm^2)$	$A_{max}(mm^2)$	$\tilde{A}_o$
200 μm	2	0.015	0.04	0.38
200 μm	4	0.001	0.08	0.02
400 μm	2	0.035	0.16	0.22
400 μm	4	0.006	0.32	0.02

(Millipore Sigma). The aqueous solution was injected into the channels at various flow rates using a syringe pump (Harvard Apparatus) to displace oil.

Videos of the intrusion of a water front and oil capture were recorded using a Nikon D850 DSLR camera equipped with a long distance working objective and a 10× magnification lens (Mitutoyo M Plan 10×0.28 Objective). The optically transparent PDMS microfluidic devices were back-lit using an LED panel. Figures 1(c)–1(f) show the progression of the intruding water front with time for representative experiments in each of the four geometries. Arrows in Figs. 1(c)–1(f) indicate the flow direction for the intruding water (blue) front, which displaces and traps oil (colorless). The direction of water motion in all subsequent figures is consistently from left to right as indicated by the arrows in Fig. 1. Image brightness and contrast of snapshots were uniformly adjusted to enhance clarity.

We determined the amount of oil remaining in each pore as well as the shape of the oil-water interface and three-phase contact angles from experimental movies using ImageJ. The oil volume was measured a few seconds after the initial trapping. There was no observable variation in the oil volume after the initial trapping in these experiments. The area of oil captured per pore is normalized to the maximum amount of oil that could fit into a given pore measured from peak to peak ($\tilde{A} = A/A_{max}$). We define the baseline amount of oil trapped in the low capillary number limit as A_o, which has previously been calculated by Gupta *et al.* as well as determined experimentally [25]. Values for A_o in our experimental geometries are reported in Table I, and were determined by averaging data points below 10^{-4}.

The typical error across experiments of similar conditions is evident from the spread of data shown in Figs. 2(e)–2(h) for $\tilde{A}$ at similar values of V_f. The maximum error measured for nearly identical conditions ($\lambda = 340$, $a = 200$ μm, $b/a = 4$ for $V_f = 2$ mm/s) was ±0.1 [Fig. 2(f)], while typical errors were ±0.065.

Oils of three different viscosities were used in these experiments. We define the ratio between the oil viscosity and water viscosity as $\lambda = \mu_o/\mu_w$ ($\mu_w = 10^{-3}$ Pa s). The oils used were Krytox General Purpose Lubricant (GPL) 102 ($\mu = 7.3 \times 10^{-2}$ Pa s, $\lambda = 73$), 103 ($\mu = 1.6 \times 10^{-1}$ Pa s, $\lambda = 160$), and 104 ($\mu = 3.4 \times 10^{-1}$ Pa s, $\lambda = 340$). Viscosity values were measured at 20 °C by the oil manufacturer [43]. The surface energy, density, and contact angles between the oil and PDMS substrate remain relatively constant across the different oils [43]. The surface tension of Krytox GPL with air is $\gamma = 17$ mN/m leading to an equilibrium contact angle on PDMS in the presence of air of approximately 7°. The interfacial tension of Krytox GPL with water is $\gamma = 53$ mN/m leading to a contact angle on PDMS in the presence of water of 42°. The three-phase contact angles for dynamic contact between PDMS, water, and Krytox reported in Fig. 5 were measured through Krytox, the denser fluid.

III. RESULTS

A. Experimental results

Previous studies using micromodels to simulate environmental porous media with interconnected porous domains found that increasing flow rates of the displacing fluid leads to a decrease in the

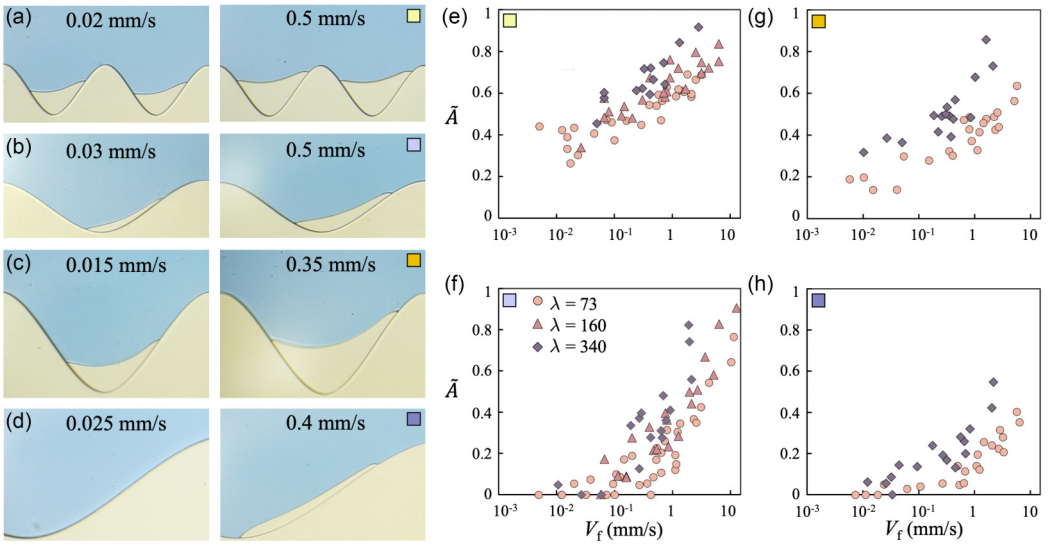

FIG. 2. More oil is trapped at higher intrusion velocity. (a)–(d) Selected experiments showing oil ($\mu_o = 7.3 \times 10^{-2}$ Pa s, $\lambda = 73$) trapped at two different intruding front velocities in pores of various geometries: (a) $a = 200\,\mu$m, $b/a = 2$, (b) $a = 200\,\mu$m, $b/a = 4$, (c) $a = 400\,\mu$m, $b/a = 2$, and (d) $a = 400\,\mu$m, $b/a = 4$. (e)–(h) Ratio of the area of trapped oil to the maximum area of each pore, $\tilde{A}$, as a function of the front velocity, V_f, for (e) $a = 200\,\mu$m, $b/a = 2$ at three different viscosity ratios (λ), (f) $a = 200\,\mu$m, $b/a = 4$ at three different values of λ, (g) $a = 400\,\mu$m, $b/a = 2$ at two different values of λ, and (h) $a = 400\,\mu$m, $b/a = 4$ at two different values of λ. Typical error between experiments are evident from measurements taken at the same value of V_f.

amount of residual oil within the three-dimensional media [37–41]. This observation was made for both cases where the displacing fluid was less wetting to the media than the displaced fluid [41] and where the displacing fluid was more wetting than the displaced fluid [39]. However, our experiments show the opposite correlation for noncontiguous cavities in quasi-two-dimensional channel flow, where increasing intrusion velocities leads to more residual oil within the pores (Fig. 2), with representative experiments shown in Figs. 2(a)–2(d). The trend between intrusion velocity and residual oil per pore is consistent across all four pore geometries [Figs. 2(e)–2(h)]. The ratio of the area of trapped oil to the maximum pore area, $\tilde{A} = A/A_{max}$, is plotted against the velocity of the water front (V_f) over four decades of speed [Figs. 2(e)–2(h)]. Our findings indicate that the amount of residual oil increases with increasing V_f for all tested geometries. Higher viscosity oils also result in more trapped oil per pore.

While overall trends remain the same across the different sinusoidal pore geometries, the amount of trapped oil is dependent on the pore geometry. Larger aspect ratio pores [$b/a = 4$, Figs. 2(b) and 2(d)] trap less oil relative to the overall pore area compared to pores with smaller aspect ratios [$b/a = 2$, Figs. 2(a) and 2(c)]. At lower front velocities ($V_f < 10^{-2}$ mm/s), we observe no oil trapped within the two $b/a = 4$ geometries, consistent with observations from Gupta *et al.* [25]. At lower flow rates and larger pore aspect ratios, oil is entirely displaced, while at larger flow rates and smaller aspect ratios, more oil remains within the pores. For all four pore geometries, the oil-water interface of the trapped phase exhibited some asymmetry, with the downstream contact line position, y_2, generally having a higher value than the upstream contact line position, y_1 [see Fig. 1(b) and Appendix E].

The fast intrusion of water into the viscous oil phase within the channels is controlled by a balance of viscous and interfacial forces. The viscosity ratio between the two fluids (λ) modulates the magnitude of drag forces across the water-oil interface and thereby dictates pressure and velocity fields in the oil phase. Surface tension forces resist drag-induced distortion of the intruding water-oil

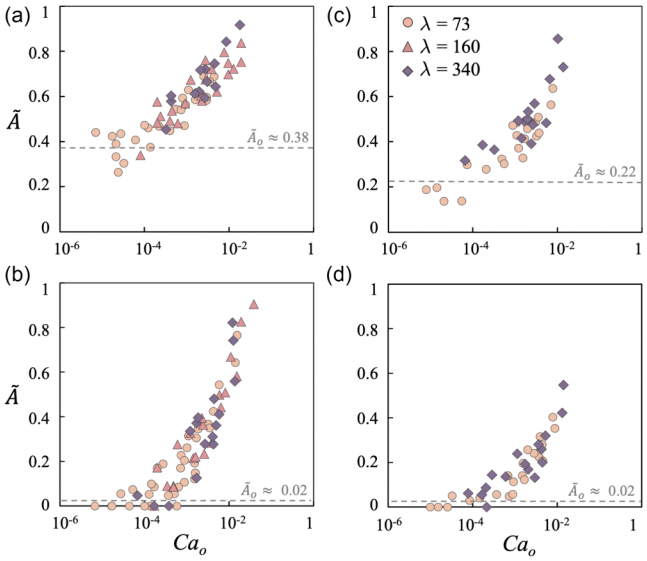

FIG. 3. Ratio of area of the trapped oil to the maximum pore area as a function of Ca_o for (a) $a = 200\,\mu m$, $b/a = 2$, (b) $a = 200\,\mu m$, $b/a = 4$, (c) $a = 400\,\mu m$, $b/a = 2$, and (d) $a = 400\,\mu m$, $b/a = 4$. The dashed gray line indicates the amount of oil remaining at the low Ca_o limit ($\tilde{A}_o$), which was previously determined by Gupta *et al.* [25].

interface. The capillary number characterizes the ratio between viscous drag in the water phase relative to surface tension forces ($Ca_o = \mu_o V_f/\gamma$). In the present problem, we find that the oil-based capillary number Ca_o primarily governs the amount of oil trapped per pore. We observe that the spread of the data for different oil viscosities collapse onto a single approximate curve upon rescaling using Ca_o (Fig. 3), suggesting that viscous dissipation in the oil is dominant in the trapping mechanism.

The amount of oil trapped in sinusoidal pores at lower capillary numbers ($Ca_o < 3 \times 10^{-5}$) where interfacial forces dominate over viscous and inertial forces was previously studied and modeled by Gupta *et al.* [25]. The theoretical predictions from that study were based on interfacial arguments incorporating both pore geometry and wettability between the three phases. Our experimental results in this zero capillary number limit are in good agreement with those predictions (see Appendix A). The minimum amount of oil trapped in our four different pore geometries as Ca_o decreases to zero (A_o) are presented in Table I. The normalized value ($\tilde{A}_o = A_o/A_{max}$) is also given.

Pore geometry plays a significant role in determining the minimum amount of oil that will be trapped in a given pore (A_o), with the smaller sinusoidal pores and smaller aspect ratio geometries being more effective at trapping oil than the larger ones. For a given flow rate of the displacing fluid, the amount of trapped oil was largest in the pores with the smaller aspect ratio ($b/a = 2$) and smallest in the pores with the larger aspect ratio ($b/a = 4$) [Fig. 4(a)]. At low values of Ca_o ($\lesssim 10^{-4}$), the amount of trapped oil approaches the zero capillary number limit given by A_o. The discrepancy between the amount of oil retained A and A_o as Ca_o increases indicates the presence of mechanisms that are not captured by a previous model for zero capillary number [25], which depends only on the pore geometry and the equilibrium contact angle, and neglects viscous forces.

A comparison of data across the different geometries is shown by Fig. 4(a), which presents the same data as Fig. 3 but differentiates between pore geometries rather than between oil viscosity. We compare the influence of Ca_o on oil trapping across the different pore geometries by subtracting the dimensionless amount of oil trapped for the zero capillary number limit, which we label $\tilde{A}_o = A_o/A_{max}$. The results for all four geometries can be collapsed onto a single trend by subtracting

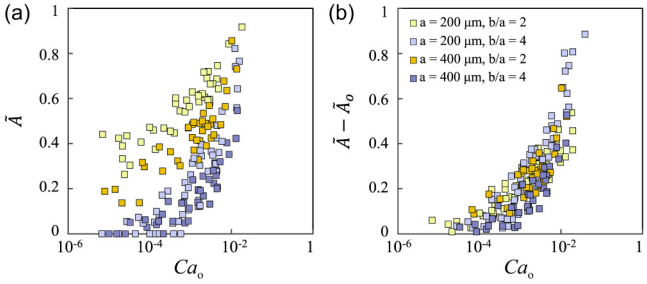

FIG. 4. (a) Dimensionless area of oil trapped as a function of capillary number for all four geometries. (b) Dimensionless area of oil trapped minus the area trapped in the low capillary number limit ($\tilde{A}_o$) as a function of capillary number for all four sine-pore geometries.

this baseline value $\tilde{A}_o$ [Fig. 4(b)]. This indicates that the dominant mechanism for trapping oil in sinusoidal pores with increasing capillary numbers is the same across all four geometries despite their differences in aspect ratio and amplitude.

The intrusion of a nonwetting fluid into a capillary prefilled with a completely wetting fluid leads to complex three phase dynamics and a velocity-dependent dynamic contact angle between the PDMS, water, and oil. In forced wetting for a partially wetting fluid, there exists some threshold velocity at which the three phase line will lose stability [44]. We investigate the relationship between three-phase dynamics and trapping in Fig. 5 and find that increasing Ca_o decreases the effective receding contact angle of the oil and thus increases the amount of oil trapped. At equilibrium, the receding contact angle of the oil phase (θ_R) between the solid PDMS and the water phase is approximately 42° [Fig. 5(a)]. However, as the flow rate and/or viscosity ratio increases, this receding contact angle decreases from its equilibrium value (see Appendix B). At the largest values of Ca_o, a thin film of oil is deposited on the flat wall such that there is no contact between the water and the solid PDMS (hence, the contact angle of the oil $\theta_R = 0$) [Fig. 5(b)].

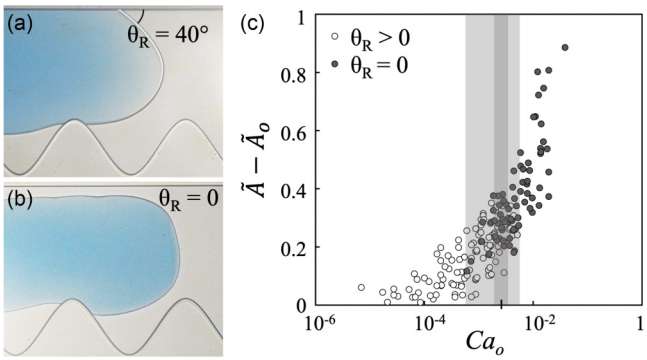

FIG. 5. Transition from triple-phase contact (meniscus) regime to viscous entrainment regime. Experimental image with (a) $Ca_o = 4 \times 10^{-4}$ for geometry $a = 200\,\mu m$, $b/a = 2$, where the dynamic receding contact angle of the oil, $\theta_R = 40°$, is close to its static value of 42°, and (b) $Ca_o = 10^{-2}$ for geometry $a = 200\,\mu m$, $b/a = 2$. Water does not contact the wall ($\theta_R \approx 0°$), and a thin film of oil is left. (c) Ratio of area of trapped oil relative to the maximum pore area minus the baseline amount as a function of Ca_o for all four geometries and all values of λ [the same data presented in Fig. 4(b)], where filled black circles indicate that $\theta_R \approx 0°$ and empty circles indicate a finite value of the receding contact angle ($\theta_R > 0$). The shaded areas indicate the full range of overlap between the two regimes (light gray) and the range where the majority (65%) of regime overlap occurs (darker gray).

The data from Fig. 4(b) are once again plotted in Fig. 5(c), this time classified into two categories: (1) experiments that exhibited a finite oil-phase receding contact angle ($\theta_R > 0$, open circles) and (2) experiments in which a thin film of oil was entrained ($\theta_R = 0$, black filled circles). A critical value of $Ca_o^\star \approx 2.3 \times 10^{-3}$ emerges at which there is a transition from a finite contact angle to no contact between the intruding water and the device wall. This transition can be considered a forced wetting transition from a meniscus regime where oil retention is approximately equal to the equilibrium values determined by thermodynamic arguments [25] to a viscous entrainment regime in which a thin layer of oil is left behind [31,33,44–47]. At lower values of Ca_o, the intrusion flow completely displaces oil from the nonpatterned wall. This regime is referred to as the meniscus regime due to the presence of a distinct three-phase contact line between the oil, water, and PDMS. As Ca_o increases, the flow transitions to a viscous entrainment regime where the lower viscosity water is surrounded by the higher viscosity oil. The thickness of the thin oil film on the flat wall in this regime matches predictions from a Bretherton-style analysis (see Appendix C) [30,47] for the thin film height entrained during immiscibile fluid-fluid displacement in a capillary channel with smooth walls. This critical value also corresponds to a dramatic increase in the slope of $\tilde{A}$ with Ca_o for all geometries due to increasing pressure in the oil phase resisting displacement.

The critical value of Ca_o found experimentally here is well matched to the value at which viscous forces are expected to become important in forced wetting transitions within a capillary [44,46]. The critical parameter for the transition from the meniscus regime with a well-defined three-phase contact line to the film regime has previously been found to be $Ca_o^\star = \theta_e^3/(9\sqrt{3}l)$ where θ_e is the equilibrium contact angle in radians, and l is a dimensionless coefficient related to the molecular length scale, and ranges from 15 to 20 for water [46,48]. For $l = 15$ and $\theta_e = 42^\circ$, $Ca_o^\star = 1.7 \times 10^{-3}$, which is well matched to the experimentally determined value of 2.3×10^{-3}. The transition region highlighted in light gray in Fig. 5(c) ranges from $Ca_o = 8 \times 10^{-4}$ to 5×10^{-3}.

B. Model results

Previous studies on entrapment in confined geometries have modeled the shape of the interface as a circular arc [25]. This purely geometric circular arc model successfully predicts the shape of the interface for lower values of capillary number where capture is independent of capillary number, and does not consider the effect of viscous forces. However, our experimental results show that the amount of trapped oil is clearly a function of the Ca_o as seen in Fig. 3. In order to account for viscous effects, we derive a model for steady-state flow using the long-wave approximation, which leverages the high geometric aspect ratio (length relative to depth) of the channel geometry (see Fig. 1) to regard the flow as approximately unidirectional. This model expands upon previous work [49] describing single-phase flows in channels with variable cross sections, where we add a second (trapped) phase delimited by an interface whose shape depends upon the flow field.

To that end, we consider a three-dimensional geometry analogous to the one used in the experiments, representing a channel of rectangular cross section with variable width [Fig. 1(a)]. One of the side walls of the channel has a sinusoidal shape given by $y = H(x)$, where x and y are the streamwise and spanwise coordinates. This texture then has a trapped fluid whose interface is given by $y = h(x)$, as shown in Fig. 6(a). We note that the fluid interface could in principle also depend on the vertical coordinate z as $y = h(x, z)$, but we assume that for moderate contact angles (sufficiently close to $\theta = 90^\circ$) neglecting the curvature around the x axis is a reasonable assumption at leading order. Following the long-wave approximation, we first nondimensionalize the streamwise coordinate x with the "long" scale b, whereas the spanwise and vertical dimensions (y, z, h, and H) are normalized with the half-depth $d/2$, the "short" scale. Furthermore, we define the geometric aspect ratios

$$\varepsilon = \frac{d}{2b}, \quad \mathcal{W} = \frac{2w}{d}, \quad \mathcal{A} = \frac{a}{d}, \tag{1}$$

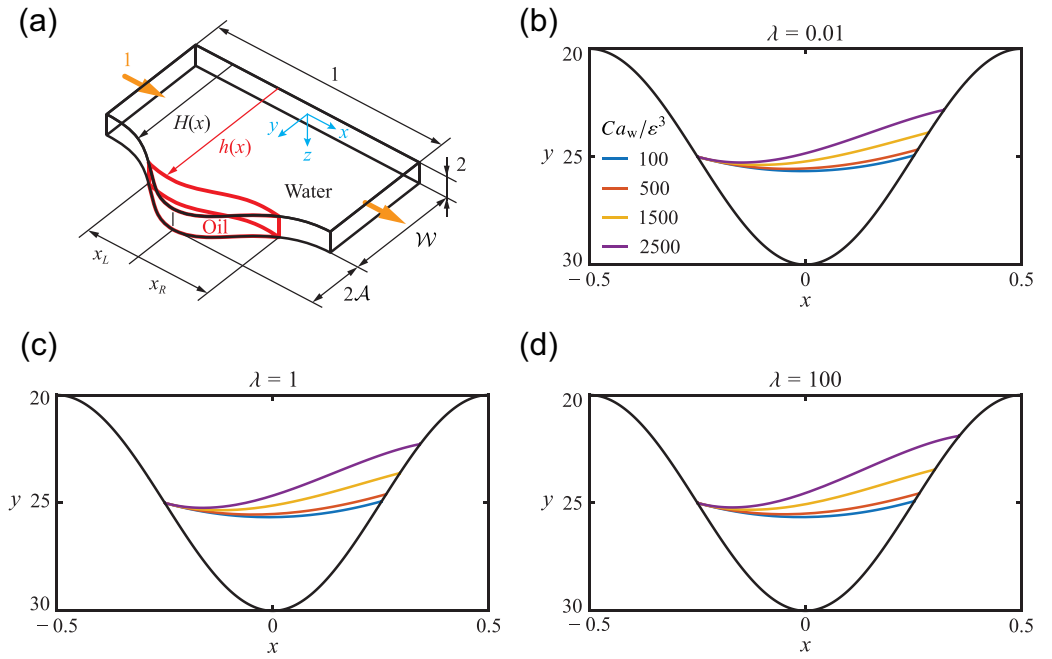

FIG. 6. Model predictions for the steady-state interface shape as a function of the water capillary number $\mathrm{Ca_w}$ and viscosity ratio λ. (a) Sketch showing the three-dimensional geometry considered in the model, where all variables have been nondimensionalized as described in Appendix D. (b)–(d) Steady-state shapes of the interface for various values of $\mathrm{Ca_w}/\varepsilon^3$ and λ, obtained from the numerical solution of Eqs. (3). The geometry of the channel is characterized by $\varepsilon = 5 \times 10^{-2}$, $\mathcal{W} = 20$, and $\mathcal{A} = 5$, which corresponds to the channel depicted in Fig. 1(c) used in the experiments. We take $\theta = 42^\circ$ for the static contact angle and $x_L = -0.25$ as an example value for the starting point of the interface. The number of modes used is $N = 16$ in all cases.

noting that typically $\varepsilon \ll 1$ in the geometry considered here. The nondimensional wall shape $H(x)$ is then

$$H(x) = \mathcal{W} + \mathcal{A}[1 + \cos(2\pi x)]. \tag{2}$$

Next, we normalize the streamwise water velocity u_w by $4Q/d^2$, where Q is the volumetric flow rate, to ensure that the nondimensional flow rate is unity, i.e., $\int_{-1}^{1}\int_{0}^{h(x)} u_\mathrm{w}\,\mathrm{d}y\,\mathrm{d}z = 1$. Applying this normalization to the Stokes equations, one can then solve an approximate version of the problem at leading order in ε^2, with details of the derivation included in Appendix D. The result is an ordinary differential equation for the interface shape, given by

$$\frac{\mathrm{d}^3 h}{\mathrm{d}x^3} = \frac{\mathrm{Ca_w}}{2\varepsilon^3}\,\frac{\mathcal{F}_1(h,H,\lambda)}{\mathcal{F}_2(h,H,\lambda)\mathcal{F}_3(h,H,\lambda) - \mathcal{F}_1(h,H,\lambda)\mathcal{F}_4(h,H,\lambda)}, \tag{3a}$$

where the lengthy functional forms of $\mathcal{F}_1(h,H,\lambda)$, $\mathcal{F}_2(h,H,\lambda)$, $\mathcal{F}_3(h,H,\lambda)$, and $\mathcal{F}_4(h,H,\lambda)$ are given by Eqs. (D17) of Appendix D, and arise from solving a cross-sectional Poisson problem through separation of variables. Here we use a capillary number $\mathrm{Ca_w} = \mu_\mathrm{w} V/\gamma = 4Q\mu_\mathrm{w}/(d^2\gamma)$ defined using the *water* viscosity (such that $\mathrm{Ca_o} = \lambda \mathrm{Ca_w}$) for convenience, since the system forcing (i.e., the prescribed flow rate) occurs for the water phase. The boundary conditions prescribe that the interface $h(x)$ and the wall $H(x)$ must intersect at the end points x_L and x_R,

$$h(x_L) = H(x_L), \tag{3b}$$

$$h(x_\mathrm{R}) = H(x_\mathrm{R}), \tag{3c}$$

and that the contact angle between the interface and the wall must be equal to θ at both ends,

$$\frac{\mathrm{d}h}{\mathrm{d}x}(x_L) = \frac{1}{\varepsilon}\tan\left[\arctan\left(\varepsilon\frac{\mathrm{d}H}{\mathrm{d}x}(x_L)\right) - \theta\right], \tag{3d}$$

$$\frac{\mathrm{d}h}{\mathrm{d}x}(x_\mathrm{R}) = \frac{1}{\varepsilon}\tan\left[\arctan\left(\varepsilon\frac{\mathrm{d}H}{\mathrm{d}x}(x_\mathrm{R})\right) + \theta\right]. \tag{3e}$$

Since we solve for the static shape of the interface, we enforce the same equilibrium contact angle at both end points, but we note that experimentally observed dynamic effects can influence the contact angle [Fig. 5(c) and Appendix B].

We numerically solve Eq. (3a) by choosing a value for the starting point x_L for the interface and treating x_R as an unknown that is obtained by imposing the four boundary conditions (3b)–(3e). Note that x_L can only be obtained from an *unsteady* analysis of the interface evolution, since it is set by the location of the moving contact line of the invading water at the instant when the water-oil interface first contacts the channel wall (see Fig. 1). Consequently, we limit this analysis to study the change in oil trapping at fixed values of x_L, and find that the model effectively captures many qualitative features found in the experiments.

Fixing the contact angle $\theta = 42^\circ$, the starting point of the interface $x_L = -0.25$, and the geometry of the channel $\varepsilon = 5 \times 10^{-2}$, $\mathcal{W} = 20$, $\mathcal{A} = 5$ [corresponding to the experiment depicted in Fig. 1(c)], we varied the $\mathrm{Ca_w}$ number of the flow for three different values of λ [Figs. 6(b) and 6(d)]. At sufficiently low $\mathrm{Ca_w}$, the interface shape $h(x)$ tends to be parabolic and symmetric around $x = 0$, which can be explained by noting that in Eq. (3a), $\frac{\mathrm{d}^3h}{\mathrm{d}x^3} \to 0$ as $\mathrm{Ca} \to 0$, which leads to a parabola. This shape is equivalent to the constant-curvature circular interface studied by Gupta *et al.* [25], which tends to a parabola in the long-wave limit. As the capillary number is increased, the interface manifests a more pronounced change of curvature and becomes asymmetric, qualitatively agreeing with the interface shapes observed in the experiments (Figs. 1 and 2). This leads to increased oil trapping, even at a fixed value for the starting point of the interface x_L.

For the geometry considered in this study, the channel is not only longer than tall ($\varepsilon \ll 1$), but also wider than tall ($\mathcal{W}, \mathcal{A} \gg 1$). Accordingly, we seek to further expand (3a) for $h, H \gg 1$ in order to potentially arrive at a useful simplified result. We note that, while rigorously expanding in several small parameters (such as ε, h^{-1}, and H^{-1}) requires fixing a relationship between them to construct asymptotically consistent expansions, here we focus only on the leading-order result, which we confirm *a posteriori* to yield an expression consistent with the solution of the complete model (3a). It is also important to note that this limit of wide channels ($h, H \gg 1$) could compromise the long-wave approximation on which the model relies, which is strictly valid when the channel length is much larger than both its width and depth [i.e., when both $\varepsilon \ll 1$ and $\varepsilon \ll (\mathcal{W} + \mathcal{A})^{-1}$]. However, in practice we can expect the model to provide a reasonable approximation even when the channel width and length are comparable, i.e., $(\mathcal{W} + \mathcal{A})^{-1} = O(\varepsilon)$, which is the case of the four geometries in the experiments. We therefore expand (3a) in the limit of $h, H \gg 1$ (see details in Appendix D), which leads to

$$\frac{\mathrm{d}^3h}{\mathrm{d}x^3} \sim \frac{3\mathrm{Ca_w}}{2\varepsilon^3}\frac{(1+\lambda)}{(1+\lambda)h + \left(\frac{186\,\zeta(5)}{\pi^5}\right)} \quad \text{for} \quad h, H \gg 1, \tag{4}$$

where $\zeta(\cdot)$ is the Riemann zeta function. It then becomes apparent that the model predicts a weak effect of the viscosity ratio λ at leading order since, for sufficiently large h,

$$\frac{\mathrm{d}^3h}{\mathrm{d}x^3} \sim \frac{3\mathrm{Ca_w}}{2\varepsilon^3 h} \quad \text{for} \quad h, H \gg 1, \tag{5}$$

or, in other words, Eq. (3a) becomes independent of λ at leading order when the width of the channel is comparable to the length of the texture. This is in agreement with the weak effect of the viscosity ratio on the overall oil trapping observed in Figs. 6(b)–6(d) for three different orders of magnitude in λ. We postulate that this weak effect is due to the high level of confinement for wide channels

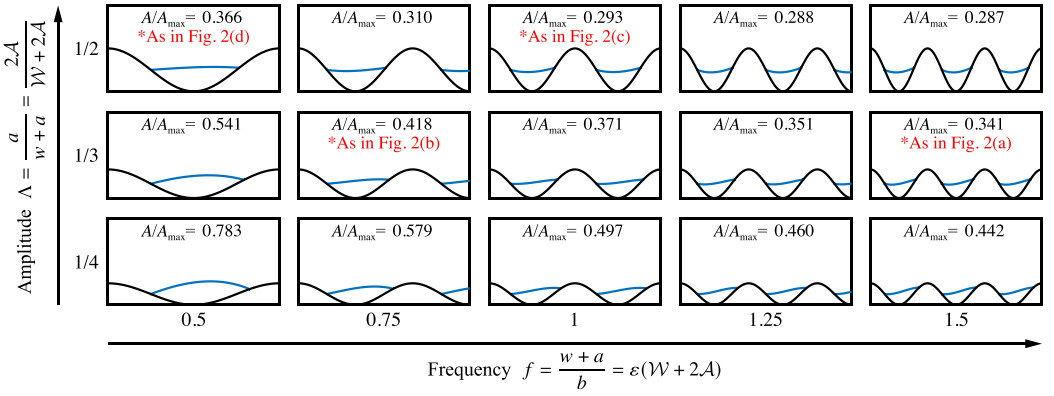

FIG. 7. Model predictions for the steady-state interface shape as a function of the texture geometry. The channel depth and width are held at $d = 40\,\mu\text{m}$ and $w = 400\,\mu\text{m}$, respectively, which is equivalent to fixing $\mathcal{W} = 20$. The amplitude a and wavelength b are varied to span a range of texture amplitudes $\Lambda = a/(w+a)$ and frequencies $f = (w+a)/b$, where cases coinciding with experimental geometries are highlighted in red. All simulations use $x_L = -0.25$, $\text{Ca}_\text{w}/\varepsilon^3 = 1500$, $\theta = 42^\circ$, $\lambda = 100$, and a number of modes truncated at $N = 16$. The predicted value A/A_max of the area of captured oil per pore, normalized by the maximum pore area, is also indicated for each case.

with $h, H \gg 1$, where the area of the oil-water interface is much smaller than the area of contact between either fluid and the channel solid walls, and therefore viscous transfer between the two phases becomes negligible. Furthermore, a scaling analysis of the simplified expression (5) reveals at which values of Ca_w one can expect the interface to transition from the parabolic shape to the asymmetric regime with more oil trapping. In this geometry, $h = O(\mathcal{W}+\mathcal{A})$ and $x = O(1)$, we estimate using (5) that the transition occurs at

$$\frac{\text{Ca}_\text{w}}{\varepsilon^3} = O[(\mathcal{W}+\mathcal{A})^2]. \tag{6}$$

This prediction is confirmed by the results in Fig. 6, where for $(\mathcal{W}+\mathcal{A}) = 25$ the interface shape only changes noticeably with respect to a symmetric parabola for values of $\text{Ca}_\text{w}/\varepsilon^3 \gg (\mathcal{W}+\mathcal{A})^2 = 625$.

While we can expect the above scaling argument to be the dominant factor determining oil trapping, the details of the texture geometry also play a role in its retention. We explore the effect of texture geometry in Fig. 7, keeping other parameters including x_L, $\text{Ca}_\text{w}/\varepsilon^3$, θ, and λ constant. Following [25], we investigate textures with varying relative amplitudes Λ, defined as $\Lambda = a/(w+a) = 2\mathcal{A}/(\mathcal{W}+2\mathcal{A})$, and varying frequencies f, where $f = (w+a)/b = \varepsilon(\mathcal{W}+2\mathcal{A})$ [see Figs. 1 and 6(a)]. We fix the effective capillary number to $\text{Ca}_\text{w}/\varepsilon^3 = 1500$ to ensure that $\text{Ca}_\text{w}/\varepsilon^3 \gtrsim (\mathcal{W}+\mathcal{A})^2$ such that oil trapping is enhanced due to interfacial deformation as shown by Eq. (6). Figure 7 illustrates that normalized oil retention $\tilde{A} = A/A_\text{max}$ increases as the relative amplitude decreases. This can be rationalized by noting that for lower amplitudes at a fixed effective capillary number, $\text{Ca}_\text{w}/\varepsilon^3$ is comparatively larger than $(\mathcal{W}+2\mathcal{A})^2$ in Eq. (6), leading to larger oil amounts trapped compared to the overall pore size. Our model also predicts a decrease in trapped oil as the frequency of the sinusoidal texture increases. This may be explained by the larger protrusion of the oil phase (which has a fixed contact angle of $\theta = 42^\circ$) for textures with smaller slopes. It is also worth noting that model predictions for the geometries explored experimentally in Figs. 2(a) and 2(c) agree qualitatively with the experimental images, albeit for a different magnitude of the capillary number [$\text{Ca}_\text{w} = O(10^{-1} - 10^{-2})$] compared to the experimental case [$\text{Ca}_\text{w} = O(10^{-6} - 10^{-4})$]. In the cases of the geometries of Figs. 2(b) and 2(d), the starting position

of the interface x_L in experiments clearly differs from $x_L = -0.25$, which makes comparisons more challenging.

While the model reproduces qualitatively the interface shapes observed in the experiments, as well as the trend of increasing oil trapping with increasing $\mathrm{Ca_w}$, it does not provide a quantitative picture. Indeed, the experimental measurements of the area of trapped oil (Fig. 2) indicate a weak yet noticeable impact of the viscosity ratio λ, whereas the model predicts a negligible effect for the experimental values of λ. Furthermore, the magnitude of $\mathrm{Ca_o} = \lambda \mathrm{Ca_w}$ for which oil trapping starts to increase noticeably in the experiments [$\mathrm{Ca_o} = O(10^{-4})$, $\mathrm{Ca_w} = O(10^{-6})$; see Fig. 3] is much lower than those predicted by the model [$\mathrm{Ca_w} = O(10^{-2})$]. We hypothesize that having the starting point of the interface x_L undetermined in the model could contribute to these discrepancies. Even though the governing equation (3a) is approximately independent of λ for wide channels with $h, H \gg 1$, the value of x_L, which is treated as an input parameter in the theory, could itself be dependent on λ in practice. This result is compatible with the experimental observation that, when $\mathrm{Ca_w}$ is increased, we typically observe that the interface starts further upstream (Fig. 2) leading to a larger amount of trapped fluid without an appreciable change in interfacial curvature.

Therefore, we emphasize that an *unsteady* analysis of the fluid invasion might be necessary to quantitatively capture the experimentally observed changes in oil trapping. The shape of the interface in such a fluid invasion problem with moving contact lines will depend on $\mathrm{Ca_w}$, λ, and θ, as is typical in drainage and imbibition problems [50,51]. In the case where the invading fluid is air, the important parameters become $\mathrm{Ca_o}$ and θ [47]. While our invading fluid is not air, it is much less viscous than the draining oil, i.e., $\lambda \gg 1$, which could explain why our experimental data is better described by $\mathrm{Ca_o} = \lambda \mathrm{Ca_w}$ rather than $\mathrm{Ca_w}$.

Discrepancies between theory and experiments could also stem from the model assumption that the interfacial curvature in the vertical direction is negligible. In other words, taking $h(x)$ instead of the more general form $h(x, z)$ [see Fig. 6(a)] is strictly valid only for contact angles $\theta = 90^\circ$ with the top and bottom channel walls, whereas in experiments $\theta = 42^\circ$. This would introduce a second interfacial curvature that would be negligible for contact angles sufficiently close to $\theta \approx 90^\circ$, but could potentially become dominant for larger deviations from 90°. The errors introduced for the experimental value $\theta = 42^\circ$ could be quantified by full numerical simulations of the multiphase problem, or using the more general functional form $h(x, z)$ in the asymptotic analysis. Since either option would introduce considerable complexity, we have restricted the analysis to a functional form $h(x)$, which still yields qualitative agreement with experiments.

IV. CONCLUSIONS

We investigated the displacement and trapping of oil in microfluidic pores by an intruding water flow and explored the influence of capillary number, viscosity ratio, and pore aspect ratio on trapping, which are dominant parameters in microfluidic multiphase flows. In contrast to results from interconnected porous media, our experimental and theoretical results for discontinuous pores reveal that the amount of trapped oil per pore increases with increasing capillary number. This result was observed for four different sinusoidal pore geometries. Increasing the wetting phase viscosity also increased fluid trapping, and we demonstrate that rescaling data with the oil-phase capillary number allows for data collapse across all oil viscosities. Data for all pore geometries can also be collapsed onto a single trend by subtracting out the amount of oil trapped in the low $\mathrm{Ca_o}$ limit ($\tilde{A}_\mathrm{o}$). Thus, the increase in oil retention with increasing values of $\mathrm{Ca_o}$ is only weakly dependent on pore geometry despite the importance of pore geometry for determining $\tilde{A}_\mathrm{o}$.

The relationship between oil trapping and $\mathrm{Ca_o}$ exhibits a transition from a meniscus displacement to a viscous displacement at a value of $\mathrm{Ca_o^\star} \approx 2.3 \times 10^{-3}$. In the mensicus displacement regime, marked by the presence of a three-phase contact line on the flat wall of the channel, there is only a modest increase in oil trapping with increasing values of $\mathrm{Ca_o}$. Following the transition to the viscous regime, there is a pronounced increase in the slope of trapped oil as a function of $\mathrm{Ca_o}$. This increase can be explained by an increase in the thickness of the dynamical oil meniscus left behind on both

the flat and the sinusoidal walls of the microfluidic device due to changing pressures imparted by the water as it quickly penetrates into the oil phase. We find that the thickness of the film left behind on the flat wall is in excellent agreement with the lubrication approximation model developed by Bretherton (see Appendix C) [30]. A similar transition from a complete displacement regime to a thin layer regime has also recently been reported for multiphase fluid displacement in Hele-Shaw devices decorated with cylindrical posts [36]. In that work, the regime was set by both the oil-phase capillary number and the ratio between the texture height and channel width.

In these experiments, the surface tension between the invading and trapped phases was held constant. Reducing surface tension by using a different oil or addition of surfactant would result in an increase in the capillary number; however, the associated amount of trapping would likely decrease. Thus, the critical capillary number reported here is likely a function of surface tension between the phases.

To rationalize experimental findings, we also developed a model for three-dimensional flow using the long-wave approximation to describe the steady-state shape of the interface and predict the amount of trapped fluid as a function of both capillary number and viscosity ratio for the sinusoidal wall of the device. Model predictions indicate that increasing water flow rates lead to more oil retention per pore, which is in agreement with experimental results. Although in good qualitative agreement with the experiments, direct quantitative comparisons with the model are limited since the model neglects the curvature of the interface into the channel and the unsteady dynamics that determine the position of the three-phase contact lines delimiting the trapped phase.

The qualitative agreement between our model and experiments allows us to better understand the underlying physics of multiphase fluid displacement and trapping within microdevice cavities. In this setting, the dominant physical effects are the capillary pressure driving the fluid interface to a state of constant curvature, and viscous drag deforming the interface and inducing asymmetry and increased trapping. Higher injection velocities (and, consequently, higher Ca_w), lead to a sharp transition in the interfacial shape that increases fluid trapping, which is observed both experimentally and in model results. At higher injection velocities, a critical value $\mathrm{Ca}_\mathrm{o} = \mathrm{Ca}_\mathrm{o}^\star$ is reached that triggers a forced wetting transition between the meniscus regime and a thin film where a continuous oil layer, reminiscent of the Bretherton problem, remains in contact with the solid walls. As capillary number continues to increase beyond the values tested here, we expect that all geometries will eventually enter a regime in which pores are completely filled ($\tilde{A} = 1$) and the oil phase forms a continuous film on both walls of the channel such that the sinusoidal cavities would be completely cloaked by oil. In such a regime with a continuous oil phase rather than discontinuous pockets of oil within disparate pores, we expect that shear flow would allow for oil drainage until continuity is broken.

ACKNOWLEDGMENTS

S.A.M. acknowledges support from the Princeton Presidential Postdoctoral Fellowship. F.T.C. acknowledges support from a Distinguished Postdoctoral Fellowship from the Andlinger Center for Energy and the Environment at Princeton University. Also, we acknowledge Sophie Roman and Amir Pahlavan for discussions on inmiscible fluid trapping in porous media. M.A.S.M., R.K., and A.J.T. received summer funding from the High Meadows Environmental Institute Environmental Internship Program at Princeton University. Microfluidic devices were fabricated via templates created using facilities at the Micro and Nano Fabrication Center cleanroom at Princeton University. Microfluidic devices were fabricated via templates created using facilities at the Micro/Nano Fabrication Center (MNFC), a core shared-use facility of the Princeton Materials Institute (PMI). The researchers at Princeton University were supported by ExxonMobil Research until January 2023.

S.A.M., F.T.C., P.R.K., R.K., A.J.T., M.A.S.M., J.S.L., and M.S.S. performed or assisted with experiments. F.T.C., P.R.K., and H.A.S. contributed to model development. A.R.K., A.J., M.S.Y., and H.A.S. conceptualized and guided the project.

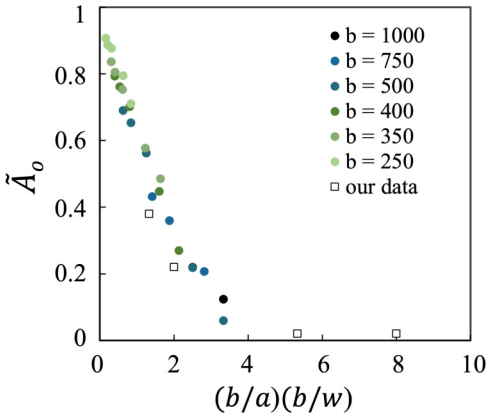

FIG. 8. Theoretical values for $\tilde{A}_o$ for various geometries studied by Gupta *et al.* [25] plotted against the product of two geometrical ratios describing the pore aspect ratio (b/a) and the aspect ratio between the pore opening (b) and the channel width (w). Experimental data from the present paper are shown by the white squares. Theoretical values were calculated using a model assuming viscous forces are negligible ($Ca_o < 10^{-4}$).

APPENDIX A: LOW Ca_o LIMIT

The amount of oil trapped in sinusoidal pores using similar microfluidic channels in the low Ca_o limit has been previously reported by Gupta *et al.* [25]. That work utilized both experiments and theory with values of Ca_o ranging between 3×10^{-5} to 3×10^{-3}, and a single value for $\lambda = 1$. The theory based on pore geometry and wettability between the three phases slightly over-predicted the amount of oil trapped in sinusoidal pores compared to experimental observations (see Gupta *et al.*, Fig. 4).

In our study, we find similar results where the theoretical predictions slightly overestimate the amount of oil trapped in the low Ca_o limit. Our notation (a, b, and w) can be translated to the dimensionless notation used in the previous work ($2m$, n, and W) via the relationships $2m = a/(w + a)$, and $n = (w + a)/b$.

The theoretical values for the dimensionless amount of oil captured in each pore in the low capillary number limit were calculated in Gupta *et al.* for a large number of pore geometries, shown by the filled circle symbols in Fig. 8. The ratio of pore wavelength to depth (b/a) multiplied by the ratio between pore wavelength and channel width (b/w) gives a geometric parameter that predicts the initial amount of oil filled in a given pore within the low capillary number limit (Fig. 8). There is a critical value of this parameter, which is about 4, at which no oil will be trapped within the pores at low values of Ca_o.

Comparing the theoretical values from Gupta *et al.* [25] with our experimental values reveals good agreement. We confirm their observation that the theory predicts overall trends but slightly overestimates oil capture. Table II compares the theoretical and experimental values for the dimensionless amount of oil captured in each pore.

TABLE II Theoretical and experimental values for dimensionless amount of oil in each pore.

a	b/a	Experimental $\tilde{A}_o$	Theory $\tilde{A}_o$
200 μm	2	0.38	0.5
200 μm	4	0.02	0.05
400 μm	2	0.22	0.32
400 μm	4	0.02	0

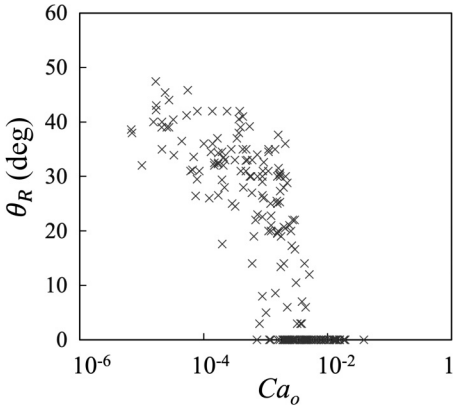

FIG. 9. Dynamic receding angle θ_R of the oil phase during displacement by the incoming water phase as function of Ca_o. Data are shown for all four pore geometries and from all three values of λ.

The same study also explored the influence of capillary numbers between ranging from 3×10^{-5} to 3×10^{-3} for a sawtooth geometry with a much smaller wavelength to depth ratio than those used here ($b/a = 0.7$). Little difference in oil capture was observed for this range of capillary numbers (equivalent to $Ca_o = 3 \times 10^{-5}$ to 3×10^{-3} for $\lambda = 1$, which are below or slightly greater than the critical value of $Ca_o^{\star} \approx 2.3 \times 10^{-3}$ found here. The geometric parameter used there was $(b/a)(b/w) = 0.19$, such that the pore was already mostly full even at the lowest value of Ca_o.

APPENDIX B: DYNAMIC CONTACT ANGLE DATA

The relationship between Ca_o and the receding contact angle of oil in the microfluidic channels is shown in Fig. 9. As Ca_o increases, the receding contact angle of oil decreases. The decrease is gradual at first, but becomes steeper around $Ca_o \approx 10^{-3}$, indicating a transition in the wetting behavior of the oil caused by the forced imbibition of water. The forced wetting transitions the flow from a three-phase capillary flow to a viscous fingering regime. The relationship between the dynamic contact angle and capillary number within small channels has been investigated in detail by others [44–47].

APPENDIX C: THIN FILM ON FLAT WALL

The thickness of the dynamical meniscus left behind on the flat wall in these experiments is in good agreement with a Bretherton-type relationship (Fig. 10). Bretherton's model predicts that the ratio between the thin film and the channel radius will be proportional to capillary number to the

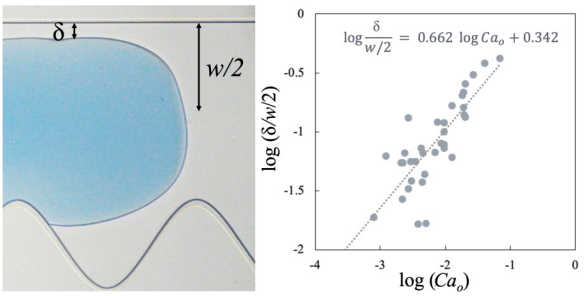

FIG. 10. A plot of $\log[\delta/(w/2)]$ vs the log of the capillary number to obtain a power-law exponent.

2/3 power: $\delta/r \approx \mathrm{Ca}^{2/3}$, where δ is the thickness of the thin film and r is the radius of the channel (here this length will be $w/2$) [30]. The experimentally determined exponent of 0.662 is in excellent agreement to the 2/3 exponent predicted by Bretherton. The modeling approach used here captures the influence of viscous stresses, just as Bretherton's model does for a straight-walled capillary tube.

Figure 10 was created using data from multiple Krytox oil viscosities and one channel geometry ($a = 200\,\mu\mathrm{m}$, $b/a = 2$).

APPENDIX D: DERIVATION OF THE MODEL

In order to derive the reduced mathematical model of Sec. III B, we start by considering the continuity

$$\nabla \cdot \boldsymbol{u}_\mathrm{o} = 0, \quad \nabla \cdot \boldsymbol{u}_\mathrm{w} = 0, \tag{D1}$$

and the Stokes equations

$$\mu_\mathrm{o} \nabla^2 \boldsymbol{u}_\mathrm{o} = \nabla p_\mathrm{o}, \quad \mu_\mathrm{w} \nabla^2 \boldsymbol{u}_\mathrm{w} = \nabla p_\mathrm{w}, \tag{D2}$$

for the oil (o) and the water (w) phases, respectively. Both fluids coexist within a periodic unit cell of a channel with a sinusoidal texture [Figs. 1(a) and 1(b)], such that $x \in [-b/2, b/2]$, $y \in [0, H(x)]$, and $z \in [-d/2, d/2]$ are the streamwise, spanwise, and vertical directions, respectively, and where $y = H(x)$ represents the sinusoidal wall and $y = h(x)$ the interface between the two phases. The velocity of each phase i can be decomposed as $\boldsymbol{u}_i = u_i \boldsymbol{e}_x + v_i \boldsymbol{e}_y + w_i \boldsymbol{e}_z$, where $\boldsymbol{e}_x$, $\boldsymbol{e}_y$, and $\boldsymbol{e}_z$ are, respectively, the unit vectors in the x, y, and z directions. The governing equations (D1) and (D2) are supplemented with no-slip boundary conditions at solid walls

$$\boldsymbol{u}_i(y = 0) = \boldsymbol{u}_i(y = H) = \boldsymbol{u}_i(z = -d/2) = \boldsymbol{u}_i(z = d/2) = 0, \tag{D3}$$

and with continuity of velocity

$$\boldsymbol{u}_\mathrm{o}(y = h) = \boldsymbol{u}_\mathrm{w}(y = h), \quad v_i(y = h) = u_i(y = h)\frac{\mathrm{d}h}{\mathrm{d}x} \tag{D4}$$

and stress

$$\left\{-(p_\mathrm{o} - p_\mathrm{w})\boldsymbol{I} + \left[\mu_\mathrm{o}\left(\nabla \boldsymbol{u}_\mathrm{o} + \nabla \boldsymbol{u}_\mathrm{o}^T\right) - \mu_\mathrm{w}\left(\nabla \boldsymbol{u}_\mathrm{w} + \nabla \boldsymbol{u}_\mathrm{w}^T\right)\right]\right\} \cdot \boldsymbol{n} = \kappa\gamma \boldsymbol{n} \tag{D5}$$

at the fluid-fluid interface, with $\boldsymbol{I}$ the identity tensor. Here the normal vector $\boldsymbol{n}$ (pointing from the water to the oil phase) and the interface curvature $\kappa = -\nabla \cdot \boldsymbol{n}$ can be obtained geometrically [52] as

$$\boldsymbol{n} = \frac{\frac{\mathrm{d}h}{\mathrm{d}x}\boldsymbol{e}_x + \boldsymbol{e}_y}{\left[1 + \left(\frac{\mathrm{d}h}{\mathrm{d}x}\right)^2\right]^{1/2}}, \quad \kappa = -\frac{\frac{\mathrm{d}^2h}{\mathrm{d}x^2}}{\left[1 + \left(\frac{\mathrm{d}h}{\mathrm{d}x}\right)^2\right]^{3/2}}. \tag{D6}$$

We also prescribe, respectively, no net flux for the (trapped) oil phase and a volumetric flow rate Q for the (flowing) water phase,

$$\int_{-d/2}^{d/2}\int_{h(x)}^{H(x)} u_\mathrm{o}\,\mathrm{d}y\,\mathrm{d}z = 0, \quad \int_{-d/2}^{d/2}\int_{0}^{h(x)} u_\mathrm{w}\,\mathrm{d}y\,\mathrm{d}z = Q. \tag{D7}$$

As outlined in Sec. III B, we rescale the problem variables following the long-wave approximation [49]:

$$x \to bx, \quad y \to \varepsilon b y, \quad z \to \varepsilon b z, \tag{D8a}$$

$$h \to \varepsilon b h, \quad H \to \varepsilon b H, \tag{D8b}$$

$$u_i \to \left(\frac{4Q}{d^2}\right)u_i, \quad v_i \to \varepsilon\left(\frac{4Q}{d^2}\right)v_i, \quad w_i \to \varepsilon\left(\frac{4Q}{d^2}\right)w_i, \tag{D8c}$$

$$p_i \to \left(\frac{4\mu_\mathrm{w} Q}{b d^2 \varepsilon^2}\right)p_i. \tag{D8d}$$

After this nondimensionalization, we retain the approximate problem at leading order in the small parameter $\varepsilon = d/(2b)$. Neglecting all higher-order terms, Eqs. (D1)–(D6) lead to Poisson problems for the oil phase,

$$\lambda\left[\frac{\partial^2 u_o}{\partial y^2} + \frac{\partial^2 u_o}{\partial z^2}\right] = \frac{dp_o}{dx}(x), \tag{D9a}$$

$$u_o(z = \pm 1) = 0, \tag{D9b}$$

$$u_o(y = H(x)) = 0, \tag{D9c}$$

and the water phase,

$$\frac{\partial^2 u_w}{\partial y^2} + \frac{\partial^2 u_w}{\partial z^2} = \frac{dp_w}{dx}(x), \tag{D10a}$$

$$u_w(z = \pm 1) = 0, \tag{D10b}$$

$$u_w(y = 0) = 0, \tag{D10c}$$

which are coupled through the continuity of velocity and tangential stress at the interface

$$u_o(y = h(x)) = u_w(y = h(x)), \tag{D11a}$$

$$\lambda\frac{\partial u_o}{\partial y}(y = h(x)) = \frac{\partial u_w}{\partial y}(y = h(x)). \tag{D11b}$$

The problem given by (D9)–(D11) can be solved using the method of separation of variables [52], since the pressure gradients on the right-hand sides of (D9) and (D10) do not depend on y or z. A lengthy calculation leads to

$$u_o(x, y, z) = -\frac{1}{\lambda}\left[\frac{dp_o}{dx}\frac{(1 - z^2)}{2} + 2\sum_{n=1}^{\infty}\frac{(-1)^n}{k_n^3}\cos(k_n z)\left\{\frac{dp_o}{dx}e^{-k_n(H-y)}\right.\right.$$
$$\left.\left. + \frac{1}{(1+\lambda)}\left[\alpha_n\frac{dp_o}{dx} - \lambda\beta_n\frac{dp_w}{dx}\right]e^{-k_n(y-h)}\left(1 - e^{-2k_n(H-y)}\right)\right\}\right], \tag{D12a}$$

$$u_w(x, y, z) = -\frac{dp_w}{dx}\frac{(1 - z^2)}{2} + 2\sum_{n=1}^{\infty}\frac{(-1)^n}{k_n^3}\cos(k_n z)\left\{-\frac{dp_w}{dx}e^{-k_n y}\right.$$
$$\left. + \frac{1}{(1+\lambda)}\left[\phi_n\frac{dp_o}{dx} - \lambda\psi_n\frac{dp_w}{dx}\right]e^{-k_n(h-y)}(1 - e^{-2k_n y})\right\}, \tag{D12b}$$

where the coefficients α_n, β_n, ϕ_n, and ψ_n are given by

$$\alpha_n(h, H, \lambda) = \frac{(1+\lambda)[\lambda e^{-k_n(H-h)}(1 - e^{-2k_n h}) + (1 - e^{-k_n(H-h)})(1 + e^{-2k_n h})]}{\lambda(1 - e^{-2k_n h})(1 + e^{-2k_n(H-h)}) + (1 + e^{-2k_n h})(1 - e^{-2k_n(H-h)})}, \tag{D13a}$$

$$\beta_n(h, H, \lambda) = \frac{(1+\lambda)(1 - e^{-k_n h})^2}{\lambda(1 - e^{-2k_n h})(1 + e^{-2k_n(H-h)}) + (1 + e^{-2k_n h})(1 - e^{-2k_n(H-h)})}, \tag{D13b}$$

$$\phi_n(h, H, \lambda) = \frac{(1+\lambda)(1 - e^{-k_n(H-h)})^2}{\lambda(1 - e^{-2k_n h})(1 + e^{-2k_n(H-h)}) + (1 + e^{-2k_n h})(1 - e^{-2k_n(H-h)})}, \tag{D13c}$$

$$\psi_n(h, H, \lambda) = \frac{(1+\lambda)[\lambda(1 - e^{-k_n h})(1 + e^{-2k_n(H-h)}) + e^{-k_n h}(1 - e^{-2k_n(H-h)})]}{\lambda[\lambda(1 - e^{-2k_n h})(1 + e^{-2k_n(H-h)}) + (1 + e^{-2k_n h})(1 - e^{-2k_n(H-h)})]}, \tag{D13d}$$

and the wave number is defined as

$$k_n = (2n - 1)\frac{\pi}{2}. \tag{D14}$$

The velocity fields given by (D12)–(D13) still contain the two undefined pressure gradient terms $\frac{\mathrm{d}p_\mathrm{o}}{\mathrm{d}x}(x)$ and $\frac{\mathrm{d}p_\mathrm{w}}{\mathrm{d}x}(x)$. Imposing the nondimensional version of the flow rates (D7),

$$\int_{-1}^{1}\int_{h(x)}^{H(x)} u_\mathrm{o}\,\mathrm{d}y\,\mathrm{d}z = 0, \qquad \int_{-1}^{1}\int_{0}^{h(x)} u_\mathrm{w}\,\mathrm{d}y\,\mathrm{d}z = 1, \tag{D15}$$

in each phase, we obtain

$$\frac{\mathrm{d}p_\mathrm{o}}{\mathrm{d}x}(x) = \frac{\mathcal{F}_1(h,H,\lambda) - \mathcal{F}_2(h,H,\lambda)}{2[\mathcal{F}_2(h,H,\lambda)\mathcal{F}_3(h,H,\lambda) - \mathcal{F}_1(h,H,\lambda)\mathcal{F}_4(h,H,\lambda)]}, \tag{D16a}$$

$$\frac{\mathrm{d}p_\mathrm{w}}{\mathrm{d}x}(x) = -\frac{\mathcal{F}_2(h,H,\lambda)}{2[\mathcal{F}_2(h,H,\lambda)\mathcal{F}_3(h,H,\lambda) - \mathcal{F}_1(h,H,\lambda)\mathcal{F}_4(h,H,\lambda)]}, \tag{D16b}$$

where the functions $\mathcal{F}_k$ are given by

$$\mathcal{F}_1(h,H,\lambda) = \frac{1}{3}(H-h) - 2\sum_{n=1}^{\infty}\frac{(1-e^{-k_n(H-h)})}{k_n^5}\left[1 + \frac{(\alpha_n - \lambda\beta_n)}{(1+\lambda)}\left(1-e^{-k_n(H-h)}\right)\right], \tag{D17a}$$

$$\mathcal{F}_2(h,H,\lambda) = \frac{1}{3}(H-h) - 2\sum_{n=1}^{\infty}\frac{(1-e^{-k_n(H-h)})}{k_n^5}\left[1 + \frac{\alpha_n}{(1+\lambda)}\left(1-e^{-k_n(H-h)}\right)\right], \tag{D17b}$$

$$\mathcal{F}_3(h,H,\lambda) = \frac{h}{3} - 2\sum_{n=1}^{\infty}\frac{(1-e^{-k_n h})}{k_n^5}\left[1 + \frac{(\lambda\psi_n - \phi_n)}{(1+\lambda)}(1-e^{-k_n h})\right], \tag{D17c}$$

$$\mathcal{F}_4(h,H,\lambda) = \frac{2}{(1+\lambda)}\sum_{n=1}^{\infty}\frac{\phi_n}{k_n^5}(1-e^{-k_n h})^2. \tag{D17d}$$

At this point in the derivation, the velocities (D12) and pressure gradients (D16) are only known as functions of the interface position $h(x)$, which is yet undetermined. The last condition to be prescribed is the normal stress jump at the interface, which in its nondimensional version yields

$$\frac{\mathrm{d}^3 h}{\mathrm{d}x^3} = \frac{\mathrm{Ca}_\mathrm{w}}{\varepsilon^3}\left(\frac{\mathrm{d}p_\mathrm{o}}{\mathrm{d}x} - \frac{\mathrm{d}p_\mathrm{w}}{\mathrm{d}x}\right), \tag{D18}$$

where the water capillary number is $\mathrm{Ca}_\mathrm{w} = \mu_\mathrm{w}V/\gamma = 4Q\mu_\mathrm{w}/(d^2\gamma)$. Combining (D18) with (D16) leads to the final reduced model (3a), which is then supplemented with boundary conditions (3b)–(3e). Once the boundary-value problem (3) is solved, the velocity fields and pressure gradients can be recovered from (D12) and (D16), respectively.

It is also worth remarking that, in the limit of large channel widths $h, H \gg 1$, we have, at leading order,

$$\alpha_n \sim 1, \quad \beta_n \sim 1, \quad \phi_n \sim 1, \quad \psi_n \sim 1, \tag{D19}$$

and, therefore, expanding the functions $\mathcal{F}_k(h,H,\lambda)$ yields

$$\mathcal{F}_1(h,H,\lambda) \sim \frac{1}{3}(H-h), \tag{D20a}$$

$$\mathcal{F}_2(h,H,\lambda) \sim \frac{1}{3}(H-h), \tag{D20b}$$

$$\mathcal{F}_3(h,H,\lambda) \sim \frac{h}{3}, \tag{D20c}$$

$$\mathcal{F}_4(h,H,\lambda) \sim \frac{62\,\zeta(5)}{\pi^5(1+\lambda)} \approx \frac{0.21}{(1+\lambda)}, \tag{D20d}$$

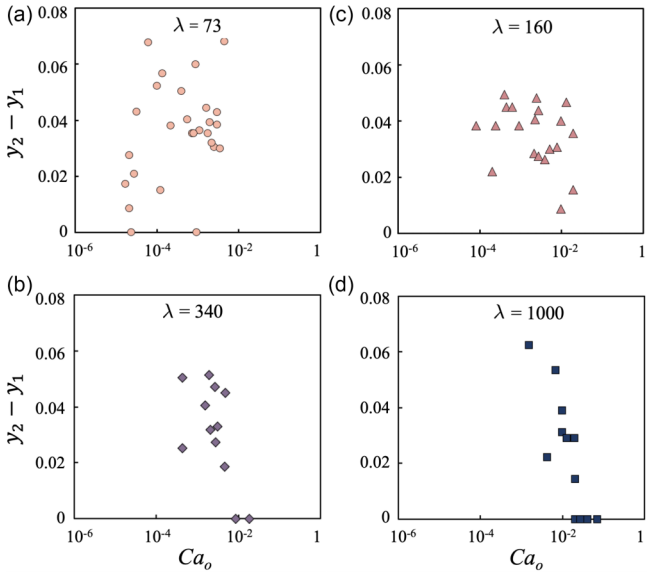

FIG. 11. Interfacial asymmetry (the difference between upstream and downstream contact line positions, $y_2 - y_1$) for geometry $a = 200$ μm, $b/a = 2$ as a function of capillary number. (a) $\lambda = 73$, (b) $\lambda = 160$, (c) $\lambda = 340$, (d) $\lambda = 1000$.

for $h, H \gg 1$, where $\zeta(\cdot)$ is the Riemann zeta function. These limit behaviors help elucidate for which values of Ca_w the oil trapping will start to grow significantly compared to the $Ca_w = 0$ case, as detailed in Sec. III B.

APPENDIX E: INTERFACE ASYMMETRY

Most experiments exhibited asymmetry across the pore water-oil interface, with the contact line position between the PDMS, water, and oil on the upstream side (y_1 in Fig. 1) typically being below the contact line position on the downstream side (y_2). This same result was reported by Gupta *et al.* [25], and this trend was observed for all geometries. For the two geometries with aspect ratio $b/a = 2$, the disparity between y_1 and y_2 was somewhat minimal [Figs. 2(c) and 2(d) and Figs. 2(a) and 2(c)] In contrast, the two geometries with aspect ratio $b/a = 4$ exhibited much larger degrees of asymmetry [Figs. 1(e) and 1(f) and Figs. 2(b) and 2(d)], with y_1 typically being 0. These results have been explained using the geometrical arguments from Gupta *et al.* via modeling the intruding interface as a circular arc [25].

We find that interfacial asymmetry (quantified as the difference between upstream and downstream contact line positions, $y_2 - y_1$) is also a function of Ca_o, but only when viscosity ratio λ is sufficiently large (Fig. 11). For $\lambda = 73$, no trend is observed [Fig. 11(a)]. For $\lambda = 160$, a trend is apparent but not particularly convincing. However, asymmetry shows a clear decrease as a function of increasing Ca_o for $\lambda = 340$ and $\lambda = 1000$ [Figs. 11(b) and 11(d)]. The Krytox 105 oil ($\mu = 1.01$ Pa s) corresponding to $\lambda = 1000$ was not included in results presented in the main text.

There are two factors contributing to this result. First is the effect of overfilling at high values of Ca_o, where pores become completely filled with oil and the difference between contact lines positions becomes zero (this occurred frequently at high values of Ca_o for $\lambda = 1000$). The second contributing factor is the influence of pressure forces in the oil phase that increase with λ to cause more asymmetry at lower Ca_o. At higher values of λ, there is significant resistance to water intrusion. Thus, at low Ca_o, the intruding front has more time to enter the pore on the upstream position (i.e., y_1 becomes small) before the front reaches the opposite peak and "pinches off" the oil to form the

contact line at position y_2. In contrast, pressure gradients in the direction of flow at low values of λ are much smaller, leading to more variation in relative contact line positions. These observations can be quantified via the increasing slopes of the plots shown in Fig. 11 with increasing viscosity ($y_2 - y_1 \sim -0.004 \log \mathrm{Ca_o}$ for $\lambda = 160$, $\sim -0.011 \log \mathrm{Ca_o}$ for $\lambda = 340$, and $\sim -0.017 \log \mathrm{Ca_o}$ for $\lambda = 1000$), and the decrease in data scatter with increasing viscosity ($R^2 = 0.37$ for $\lambda = 160$, $R^2 = 0.50$ for $\lambda = 340$, and $R^2 = 0.80$ for $\lambda = 1000$).

[1] K. Singh, M. Jung, M. Brinkmann, and R. Seemann, Capillary-dominated fluid displacement in porous media, Annu. Rev. Fluid Mech. **51**, 429 (2019).

[2] H. A. Stone, A. D. Stroock, and A. Ajdari, Engineering flows in small devices: Microfluidics toward a lab-on-a-chip, Annu. Rev. Fluid Mech. **36**, 381 (2004).

[3] J. D. Smith, R. Dhiman, S. Anand, E. Reza-Garduno, R. E. Cohen, G. H. McKinley, and K. K. Varanasi, Droplet mobility on lubricant-impregnated surfaces, Soft Matter **9**, 1772 (2013).

[4] A. Lafuma and D. Quéré, Slippery pre-suffused surfaces, Europhys. Lett. **96**, 56001 (2011).

[5] M. S. Yeganeh, A. Jusufi, S. P. Deighton, M. S. Ide, M. Siskin, A. Jaishankar, C. Maldarelli, P. Bertolini, B. Natarajan, J. L. Vreeland, M. A. King, and A. R. Konicek, Solid with infused reactive liquid (SWIRL): A novel liquid-based separation approach for effective CO_2 capture, Sci. Adv. **8**, eabm0144 (2022).

[6] B. R. Solomon, K. S. Khalil, and K. K. Varanasi, Drag reduction using lubricant-impregnated surfaces in viscous laminar flow, Langmuir **30**, 10970 (2014).

[7] S. A. McBride, S. Dash, and K. K. Varanasi, Evaporative crystallization in drops on superhydrophobic and liquid-impregnated surfaces, Langmuir **34**, 12350 (2018).

[8] H.-L. Girard, P. Bourrianne, M. Yeganeh, R. E. Cohen, G. H. McKinley, and K. K. Varanasi, Lubricant-impregnated surfaces for mitigating asphaltene deposition, ACS Appl. Mater. Interfaces **12**, 28750 (2020).

[9] G. S. Bakken, M. R. Banta, C. M. Higginbotham, and A. J. Lynott, It's just ducky to be clean: The water repellency and water penetration resistance of swimming mallard *Anas platyrhynchos* ducklings, J. Avian Biol. **37**, 561 (2006).

[10] K. K. Mohanty, H. T. Davis, and L. E. Scriven, Physics of oil entrapment in water-wet rock, SPE Res. Eng. **2**, 113 (1987).

[11] H. Lee, R. L. Srinivas, A. Gupta, and P. S. Doyle, Sensitive and multiplexed on-chip microRNA profiling in oil-isolated hydrogel chambers, Angew. Chem. Int. Ed. **54**, 2477 (2015).

[12] A. M. Foudeh, T. Fatanat Didar, T. Veres, and M. Tabrizian, Microfluidic designs and techniques using lab-on-a-chip devices for pathogen detection for point-of-care diagnostics, Lab Chip **12**, 3249 (2012).

[13] S. G. Lee, H. Lee, A. Gupta, S. Chang, and P. S. Doyle, Site-selective in situ grown calcium carbonate micromodels with tunable geometry, porosity, and wettability, Adv. Funct. Mater. **26**, 4896 (2016).

[14] P. Abbyad, R. Dangla, A. Alexandrou, and C. N. Baroud, Rails and anchors: Guiding and trapping droplet microreactors in two dimensions, Lab Chip **11**, 813 (2011).

[15] C. Chalbaud, M. Robin, J.-M. Lombard, F. Martin, P. Egermann, and H. Bertin, Interfacial tension measurements and wettability evaluation for geological CO_2 storage, Adv. Water Resour. **32**, 98 (2009).

[16] Z. T. Karpyn, M. Piri, and G. Singh, Experimental investigation of trapped oil clusters in a water-wet bead pack using X-ray microtomography, Water Resour. Res. **46**, 2008WR007539 (2010).

[17] M. Kang, W. Park, S. Na, S.-M. Paik, H. Lee, J. W. Park, H.-Y. Kim, and N. L. Jeon, Capillarity guided patterning of microliquids, Small **11**, 2789 (2015).

[18] M. H. Schneider and P. Tabeling, Lab-on-chip methodology in the energy industry: Wettability patterns and their impact on fluid displacement in oil reservoir models, Am. J. Appl. Sci. **8**, 927 (2011).

[19] P. K. Mondal, D. Das Gupta, and S. Chakraborty, Interfacial dynamics of two immiscible fluids in spatially periodic porous media: The role of substrate wettability, Phys. Rev. E **90**, 013003 (2014).

[20] H. Lee, A. Gupta, T. A. Hatton, and P. S. Doyle, Creating isolated liquid compartments using photopatterned obstacles in microfluidics, Phys. Rev. Appl. **7**, 044013 (2017).

[21] M. Jung, M. Brinkmann, R. Seemann, T. Hiller, M. Sanchez de La Lama, and S. Herminghaus, Wettability controls slow immiscible displacement through local interfacial instabilities, Phys. Rev. Fluids **1**, 074202 (2016).
[22] N. R. Morrow, *Interfacial Phenomena in Petroleum Recovery* (OSTI, New York, 1991).
[23] T. M. Squires and S. R. Quake, Microfluidics: Fluid physics at the nanoliter scale, Rev. Mod. Phys. **77**, 977 (2005).
[24] G. R. Jerauld and S. J. Salter, The effect of pore-structure on hysteresis in relative permeability and capillary pressure: Pore-level modeling, Transp. Porous Media **5**, 103 (1990).
[25] A. Gupta, H. Lee, and P. S. Doyle, Controlled liquid entrapment over patterned sidewalls in confined geometries, Phys. Rev. Fluids **2**, 094007 (2017).
[26] Y. Liu, J. S. Wexler, C. Schönecker, and H. A. Stone, Effect of viscosity ratio on the shear-driven failure of liquid-infused surfaces, Phys. Rev. Fluids **1**, 074003 (2016).
[27] J. S. Wexler, A. Grosskopf, M. Chow, Y. Fan, I. Jacobi, and H. A. Stone, Robust liquid-infused surfaces through patterned wettability, Soft Matter **11**, 5023 (2015).
[28] S. Roman, C. Soulaine, and A. R. Kovscek, Pore-scale visualization and characterization of viscous dissipation in porous media, J. Colloid Interface Sci. **558**, 269 (2020).
[29] S. Ji, H. Li, Z. Du, P. Lv, and H. Duan, Influence of interfacial coupled flow on slip boundary over a microstructured surface, Phys. Rev. Fluids **8**, 054003 (2023).
[30] F. P. Bretherton, The motion of long bubbles in tubes, J. Fluid Mech. **10**, 166 (1961).
[31] C. Huh and L. E. Scriven, Hydrodynamic model of steady movement of a solid/liquid/fluid contact line, J. Colloid Interface Sci. **35**, 85 (1971).
[32] R. J. Hansen and T. Y. Toong, Dynamic contact angle and its relationship to forces of hydrodynamic origin, J. Colloid Interface Sci. **37**, 196 (1971).
[33] E. J. Soares, M. S. Carvalho, and P. R. S. Mendes, Immiscible liquid-liquid displacement in capillary tubes, J. Fluids Eng. **127**, 24 (2005).
[34] A. Gupta, H. Lee, and P. S. Doyle, Oil recovery from micropatterned triangular troughs during a surfactant flood, Langmuir **34**, 10644 (2018).
[35] M. S. Kamal, I. A. Hussein, and A. S. Sultan, Review on surfactant flooding: Phase behavior, retention, IFT, and field applications, Energy Fuels **31**, 7701 (2017).
[36] Y. Qiu, K. Xu, A. A. Pahlavan, and R. Juanes, Wetting transition and fluid trapping in a microfluidic fracture, Proc. Natl. Acad. Sci. USA **120**, e2303515120 (2023).
[37] A. Q. Raeini, B. Bijeljic, and M. J. Blunt, Modelling capillary trapping using finite-volume simulation of two-phase flow directly on micro-CT images, Adv. Water Resour. **83**, 102 (2015).
[38] R. Lenormand and C. Zarcone, Role of roughness and edges during imbibition in square capillaries, in *SPE Annual Technical Conference and Exhibition*, SPE–13264 (SPE, Houston, TX, 1984).
[39] S. S. Datta, T. S. Ramakrishnan, and D. A. Weitz, Mobilization of a trapped non-wetting fluid from a three-dimensional porous medium, Phys. Fluids **26**, 022002 (2014).
[40] E. Aspenes, G. Ersland, A. Graue, J. Stevens, and B. A. Baldwin, Wetting phase bridges establish capillary continuity across open fractures and increase oil recovery in mixed-wet fractured chalk, Transp. Porous Media **74**, 35 (2008).
[41] Y. Wang, C. Zhang, N. Wei, M. Oostrom, T. W. Wietsma, X. Li, and A. Bonneville, Experimental study of crossover from capillary to viscous fingering for supercritical CO_2–water displacement in a homogeneous pore network, Environ. Sci. Technol. **47**, 212 (2013).
[42] V. I. Astafev and A. E. Kasatkin, Modeling and numerical calculation of piston-like oil displacement for doubly-periodic systems of oil fields development, in *COUPLED VI: Proceedings of the VI International Conference on Computational Methods for Coupled Problems in Science and Engineering* (CIMNE, 2015), pp. 734–742.
[43] Chemours Company, *Krytox General Purpose Lubricants Performance Lubricants Product Information*, brochure (Chemours Company, Wilmington, 2017).
[44] R. L. Hoffman, A study of the advancing interface. I. Interface shape in liquid–gas systems, J. Colloid Interface Sci. **50**, 228 (1975).

[45] C. G. Ngan and E. B. Dussan V, On the nature of the dynamic contact angle: An experimental study, J. Fluid Mech. **118**, 27 (1982).

[46] P.-G. de Gennes, F. Brochard-Wyart, and D. Quere, Dynamics of the triple line, in *Capillarity and Wetting Phenomena: Drops, Bubbles, Pearls, Waves* (Springer, New York, 2015), pp. 734–742.

[47] B. Zhao, A. Alizadeh Pahlavan, L. Cueto-Felgueroso, and R. Juanes, Forced wetting transition and bubble pinch-off in a capillary tube, Phys. Rev. Lett. **120**, 084501 (2018).

[48] P. G. de Gennes, Wetting: Statics and dynamics, Rev. Mod. Phys. **57**, 827 (1985).

[49] E. Lauga, A. D. Stroock, and H. A. Stone, Three-dimensional flows in slowly varying planar geometries, Phys. Fluids **16**, 3051 (2004).

[50] B. Levaché and D. Bartolo, Revisiting the Saffman-Taylor experiment: Imbibition patterns and liquid-entrainment transitions, Phys. Rev. Lett. **113**, 044501 (2014).

[51] B. K. Primkulov, A. A. Pahlavan, X. Fu, B. Zhao, C. W. MacMinn, and R. Juanes, Wettability and Lenormand's diagram, J. Fluid Mech. **923**, A34 (2021).

[52] L. Leal, *Advanced Transport Phenomena: Fluid Mechanics and Convective Transport Processes* (Cambridge University Press, Cambridge, 2007).